Journal of Materials Chemistry A

ROYAL SOCIETY OF CHEMISTRY

PAPER

View Article Online
View Journal | View Issue

Cite this: J. Mater. Chem. A, 2026, 14, 9324

Efficient ammonia synthesis *via* electrocatalytic nitrate reduction over a [8 + 2]-connected three-dimensional metal-bipyridine covalent organic framework

Tsukasa Irie, †[a] Ayumu Kondo,†[a] Kai Sun,†[b] Kohki Sasaki,[a] Mika Nozaki,[a] Shiho Tomihari,[a] Kotaro Sato,[c] Tokuhisa Kawawaki, [a] Yu Zhao, *[d] Saikat Das *[a] and Yuichi Negishi *[a]

Covalent organic frameworks (COFs) have recently emerged as promising platforms for electrocatalytic nitrate reduction to ammonia (NO_3RR), yet most reported systems are limited to two-dimensional architectures. Herein, we present TU-82, a structurally distinct 3D COF featuring an intricate [8 + 2]-connected **bcu** topology derived from the reticulation of an octatopic D_{2h}-symmetric tetragonal prism node and a C_2-symmetric bipyridyl linker. TU-82 exhibits high crystallinity, permanent porosity, and robust structural integrity, enabling precise postsynthetic metalation at bipyridyl coordination sites to yield catalytically active TU-82-Fe and TU-82-Cu frameworks. Among them, TU-82-Fe demonstrates superior NO_3RR performance, delivering a faradaic efficiency (FE) of 88.1% at −0.6 V (RHE) and an ammonia yield rate of 2.87 mg h^{-1} cm^{-2} at −0.8 V (RHE), together with a turnover frequency of 7.2 h^{-1} and excellent operational stability. Density functional theory calculations reveal that the enhanced activity of TU-82-Fe originates from a lower energy barrier (0.354 eV) for the rate-determining NO* → NHO* step along the NHO-mediated reaction pathway. This work pioneers a structural blueprint for deploying 3D COFs in electrocatalysis, fostering deeper insights into framework-controlled reactivity and offering new routes to sustainable nitrate management.

Received 29th September 2025
Accepted 12th December 2025

DOI: 10.1039/d5ta07989f

rsc.li/materials-a

1. Introduction

Ammonia (NH_3) is an indispensable chemical for fertilizers, pharmaceuticals, and emerging energy technologies due to its high hydrogen content (17.6 wt%) and carbon-free nature.[1,2] Despite its central role, industrial ammonia synthesis remains dominated by the Haber–Bosch (HB) process, a century-old method responsible for about 1.5–2.0% of global CO_2 emissions and consuming about 2% of the world's energy supply.[3] In contrast, the electrochemical nitrate reduction reaction (NO_3RR) has gained momentum as a green and decentralized strategy for ammonia synthesis.[4] Not only does NO_3RR bypass the high-pressure, high-temperature conditions of the HB process, but it also addresses the global nitrate pollution crisis by converting NO_3^-, a common contaminant from agricultural runoff and industrial waste, into value-added NH_3.[5] Compared to N_2, NO_3^- is more soluble, chemically reactive, and easier to reduce due to its lower bond dissociation energies.[6] Furthermore, recent innovations in plasma and oxidation chemistry have enabled the efficient oxidation of atmospheric N_2 into nitrogen oxides (NO_x), which can be further transformed into stable nitrate feedstocks.[7] Therefore, electrochemical NO_3RR offers a dual benefit of sustainable ammonia generation and environmental remediation, positioning it as a key technology for a circular nitrogen economy.

Efficient NO_3RR is an eight-electron, nine-proton process complicated by sluggish kinetics and competition with the hydrogen evolution reaction (HER), necessitating the development of robust and selective catalysts.[8] A wide range of catalyst systems has been explored to date, including metal nanoparticles, alloys, metal oxides/hydroxides, nanoclusters, single-atom catalysts (SACs), and molecular complexes.[9,10] Metal nanoparticles and alloys have been among the earliest and most extensively investigated materials. Bimetallic catalysts such as

[a]Institute of Multidisciplinary Research for Advanced Materials, Tohoku University, 2-1-1 Katahira, Aoba-ku, Sendai 980-8577, Japan. E-mail: das.saikat.c4@tohoku.ac.jp; yuichi.negishi.a8@tohoku.ac.jp

[b]Department School of Materials and Energy, and LONGi Institute of Future Technology, Lanzhou University, Lanzhou 730000, China

[c]Carbon Value Research Center, Research Institute for Science & Technology, Tokyo University of Science, Kagurazaka, Shinjuku-ku, Tokyo 162-8601, Japan

[d]Zhejiang Engineering Laboratory for Green Syntheses and Applications of Fluorine-Containing Specialty Chemicals, Institute of Advanced Fluorine-Containing Materials, Zhejiang Normal University, 321004 Jinhua, China. E-mail: zhaoyu@zjnu.edu.cn

† These authors contributed equally.

Ni–Cu, Ru–Cu, and Pd–Ru have shown synergistic effects that enhance NO_3^- adsorption, intermediate stabilization, and NH_3 selectivity.[11] For instance, Liu *et al.* reported a PdCu alloy catalyst that achieved an impressive NH_3 faradaic efficiency (FE) of 85% and an NH_3 yield rate of 3058 μg h^{-1} mg^{-1} at −0.25 V *vs.* reversible hydrogen electrode (RHE).[12] Cu–Pt nanostructure developed by Das *et al.* achieved a FE of 72.33% for NH_3 at −0.1 V *vs.* RHE, along with substantial ammonia output of 0.71 mg h^{-1} mg_{cat}^{-1} at −0.3 V.[13] Metal oxides and hydroxides, such as TiO_2, Fe_3O_4, and Cu_2O, offer distinct advantages due to their structural stability and redox-active surfaces. For example, Zhang and colleagues reported that TiO_2 nanotubes exhibited an FE of 66.3% and an NH_3 yield of 0.024 mmol h^{-1} mg^{-1}, which increased to 85.0% and 0.045 mmol h^{-1} mg^{-1}, respectively, upon introducing oxygen vacancies.[14] However, these materials often suffer from limited conductivity and moderate catalytic turnover rates, which has motivated the exploration of more tunable systems. Metal nanoclusters, such as Cu_{14} developed by our group, achieved 78% FE at −0.4 V *vs.* RHE—2.7 times higher than counterparts without exposed Cu sites and over 5.6 times greater than conventional Cu nanoparticles.[15] SACs represent a breakthrough in NO_3RR electrocatalysis due to their atomically dispersed metal sites, which maximize active site utilization and often exhibit unique reaction pathways. Fe SACs on nitrogen-doped carbon, prepared *via* two-step pyrolysis, showed ∼75% FE with enhanced NH_3 selectivity attributed to the suppression of N–N coupling.[16] However, pyrolytic methods often lead to uncontrolled coordination environments, low metal loading, and defect-rich supports, hindering the establishment of clear structure-activity relationships. Molecular electrocatalysts, including porphyrins and phthalocyanines, offer a complementary approach by combining well-defined coordination environments with structural modularity.[17] Their rigid π-conjugated backbones can stabilize isolated transition metals and facilitate selective nitrate-to-ammonia conversion. These systems allow for precise tuning of the metal center electronic structure and have the added advantage of synthetic accessibility and compositional versatility. However, drawbacks include aggregation of the active molecules under operating conditions, limited conductivity, and challenges in immobilization on electrodes. Collectively, while substantial progress has been made in designing NO_3RR catalysts, limitations such as poor structural tunability, low active site exposure, and insufficient control over coordination environments persist across most systems. This underscores the need for new catalyst platforms that combine structural modularity, high porosity, programmable active site integration, and long-range order.

Covalent organic frameworks (COFs) are an emerging class of crystalline, porous polymers built from reticulated organic building blocks *via* strong covalent bonds.[18–31] Their high surface areas, ordered porosity, and modular backbones make them ideal scaffolds for incorporating redox-active moieties and coordinating catalytic centers in well-defined environments. COFs have already demonstrated their potential in electrocatalysis, particularly in CO_2 reduction, oxygen evolution, and hydrogen evolution reactions. In 2015, Yaghi *et al.* first demonstrated that metalloporphyrin-based COFs could serve as efficient electrocatalysts for CO_2 reduction, highlighting the advantages of site isolation, periodicity, and framework stability.[32] More recently, the potential of COFs for NO_3RR has garnered growing attention. Most of the reported examples are two-dimensional (2D) COFs constructed from metal-porphyrin or metal-bipyridine linkers.[33–39] Lu and co-workers developed a series of metal-porphyrin COFs, where Fe−, Co−, Ni, and Cu-centered porphyrin nodes were incorporated into 2D layered frameworks.[33] These COFs achieved FEs of up to 85.4% for NH_3 and an ammonia yield rate of 1883.6 μmol h^{-1} mg^{-1} COF, with high selectivity attributed to the suppression of N–N coupling and stabilization of key NO_3RR intermediates. Similarly, Li *et al.* developed a highly crystalline, mesoporous 2D nickel porphyrin COF (NiPr-TPA-COF) that exhibited ∼90% NH_3 selectivity, a production rate of 2.5 mg h^{-1} cm^{-2}, and a turnover frequency (TOF) of 3.5 s^{-1} for electrochemical nitrate reduction in neutral media.[34] Nejati *et al.* developed a vapor-phase strategy to construct Cu- and Co-porphyrin COFs, with CuPOR-COF achieving a peak FE of *ca.* 86% and an NH_3 production rate of 6.0 mg h^{-1} cm^{-2} under an applied potential range of −1.4 to −1.8 V *vs.* Ag/AgCl.[35] In parallel, metal-bipyridine COFs have also emerged as promising NO_3RR catalysts, offering a more compact and modular metal-binding environment compared to porphyrins. For instance, Lu and co-workers synthesized isomeric bipyridine-based COFs, incorporating Fe, Co, or Ni ions within mesoporous 2D backbones.[36] Identified as the most efficient for electrocatalytic nitrate reduction, the Fe-coordinated framework (Py-Bpy-Fe) achieved 91.2% FE at −1.6 V *vs.* SCE and ∼3909 μmol h mg^{-1} NH_3 yield at −2.0 V *vs.* SCE. A structural isomer with dual bipyridine sites (Py-PyIm-Fe) further boosted the NH_3 yield to ∼4300 μmol h^{-1} mg^{-1}. These frameworks benefit from the ability to precisely localize metal centers within a tunable π-conjugated system, which facilitates efficient electron transport and substrate activation. However, despite their promise, most COF-based NO_3RR catalysts reported to date remain confined to 2D architectures. In contrast, three-dimensional (3D) COFs remain virtually unexplored for NO_3RR, representing an untapped frontier with transformative potential. Unlike their 2D counterparts, which often suffer from interlayer π–π stacking that can restrict ion diffusion and reduce site accessibility, 3D COFs feature an extended framework that allows isotropic diffusion of electrolyte ions and uniform exposure of active sites. The inherently higher connectivity and crosslinking in 3D COFs enhances structural robustness, charge delocalization, and mechanical stability under electrochemical conditions. Furthermore, their topological diversity enables the integration of high densities of metal-binding sites within a rigid and spatially addressable scaffold. High-connectivity 3D nets, such as **bcu**, **pts**, **ffc**, or **scu**, are particularly appealing for NO_3RR, as they provide interconnected channels that facilitate reactant transport and enable cooperative catalysis through spatially ordered active sites. Importantly, the precise and periodic positioning of these sites enables better understanding of structure–activity relationships, which is often elusive in amorphous or disordered systems. Despite these advantages, only one 3D COF has been

recently reported for NO_3RR,[40] underscoring the nascency of this field and revealing a critical gap in current catalyst development strategies. Bridging this gap offers the potential to not only improve catalytic performance but also unlock new mechanistic insights through rational framework engineering.

In this study, we report a topologically intricate 3D COF as an electrocatalyst for selective nitrate-to-ammonia transformation. The COF, termed TU-82, is built through [8 + 2] topological design by integrating a D_{2h}-symmetric octatopic tetragonal prismatic building unit and a C_2-symmetric bipyridyl linker, establishing a highly ordered, intrinsically porous three-periodic **bcu** network. The COF's bipyridyl pockets facilitate controlled metal coordination, enabling generation of Fe- and Cu-functionalized analogues with well-defined active centers. Exhibiting robust performance metrics toward nitrate reduction, TU-82-Fe outperforms its Cu analogue, exhibiting an impressive FE of 88.1% (at −0.6 V *vs.* RHE), elevated NH_3 productivity of 2.87 mg h^{-1} cm^{-2} (at −0.8 V *vs.* RHE), and prolonged cycling stability. Mechanistic modeling reveals that both Fe and Cu sites favor the NHO-mediated reduction pathway, with the Fe center offering a lower activation barrier (0.354 eV) for the rate-determining step (NO* → NHO*). This study not only introduces a new design paradigm by leveraging the structural precision and connectivity of 3D COFs but also sets the stage for understanding structure–activity relationships in reticular electrocatalysts. The findings open avenues for developing next-generation, architecturally programmable COF-based catalysts for sustainable nitrogen cycle engineering.

2. Results and discussion

The 3D COF TU-82 was synthesized *via* a solvothermal Schiff-base condensation reaction between 4′,5′-bis(3,5-diformylphenyl)-3′,6′-dimethyl-[1,1′:2′,1″-terphenyl]-3,3″,5,5″-tetracarbaldehyde (DPTB-Me) and 2,2′-bipyridine-5,5′-diamine (Bpy), in a 1 : 4 molar ratio. Optimal reaction conditions were identified following extensive parameter screening, wherein a mixed solvent system of *o*-dichlorobenzene and *n*-butanol (1 : 3, v/v), with 6 M aqueous acetic acid as the catalyst, afforded TU-82 as a yellow crystalline solid after heating at 120 °C for 72 h (Fig. 1a). The incorporation of bipyridine moieties within the framework was strategic, enabling postsynthetic metalation due to their strong chelating affinity for transition metals—a critical feature for engineering catalytically competent sites in electrocatalytic NO_3RR (Fig. 1c and d). Postsynthetic coordination with Fe^{2+} and Cu^{+}/Cu^{2+} ions was achieved by refluxing TU-82 in methanolic solutions of the corresponding metal acetates at 60 °C for 12 h under an inert argon atmosphere, yielding TU-82-Fe and TU-82-Cu, respectively (Fig. 1a). Crystallographic elucidation of TU-82 was accomplished through detailed analysis of powder X-ray diffraction (PXRD) data in comparison with simulated patterns derived from energy-minimized structural

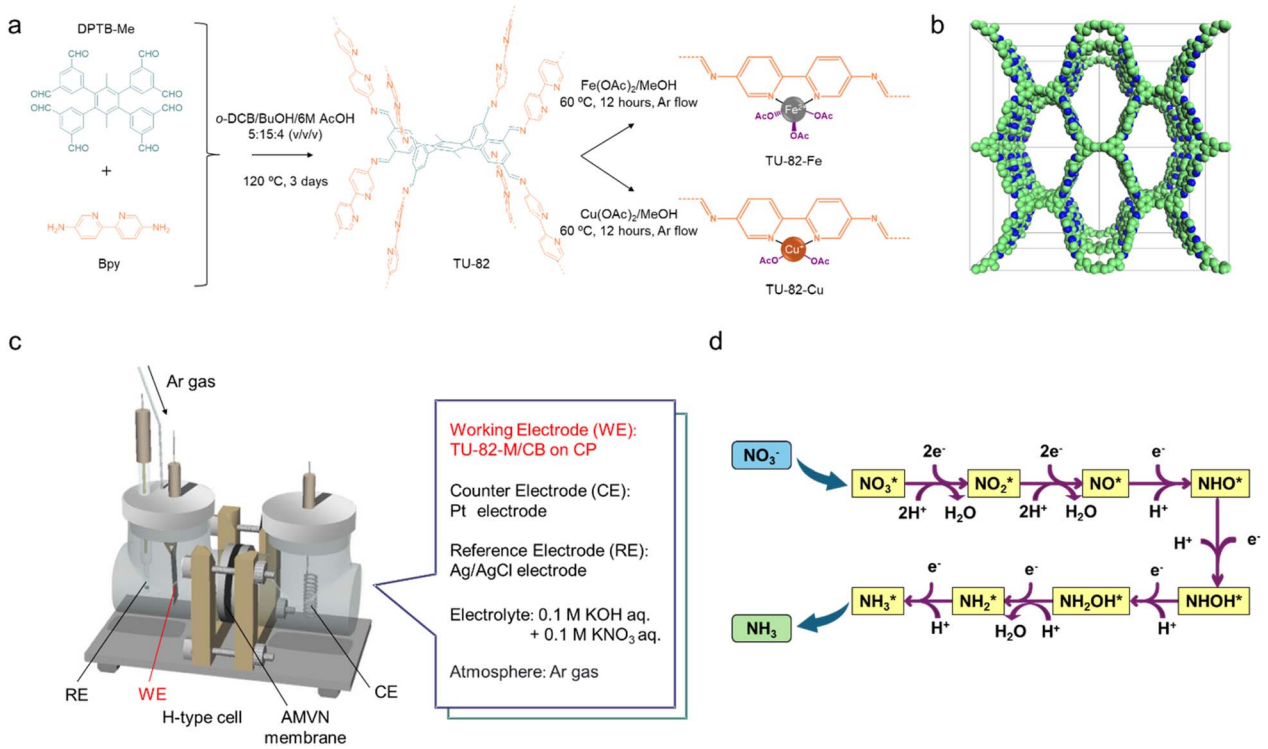

Fig. 1 (a) Synthesis of 3D COF TU-82 with a [8 + 2]-connected **bcu** topology *via* condensation of DPTB-Me and Bpy, followed by postsynthetic metalation with Fe^{2+} or $Cu^{+/2+}$ in methanol at 60 °C to afford TU-82-M (M = Fe, Cu). (b) Extended structure of non-interpenetrated bcu net of TU-82. (c) Schematic of the electrochemical nitrate reduction reaction (NO_3RR) setup, showing the working electrode, electrolyte composition, and cell configuration. (d) Proposed reaction pathway for the electrochemical conversion of nitrate (NO_3^-) to ammonia (NH_3) catalyzed by TU-82-M.

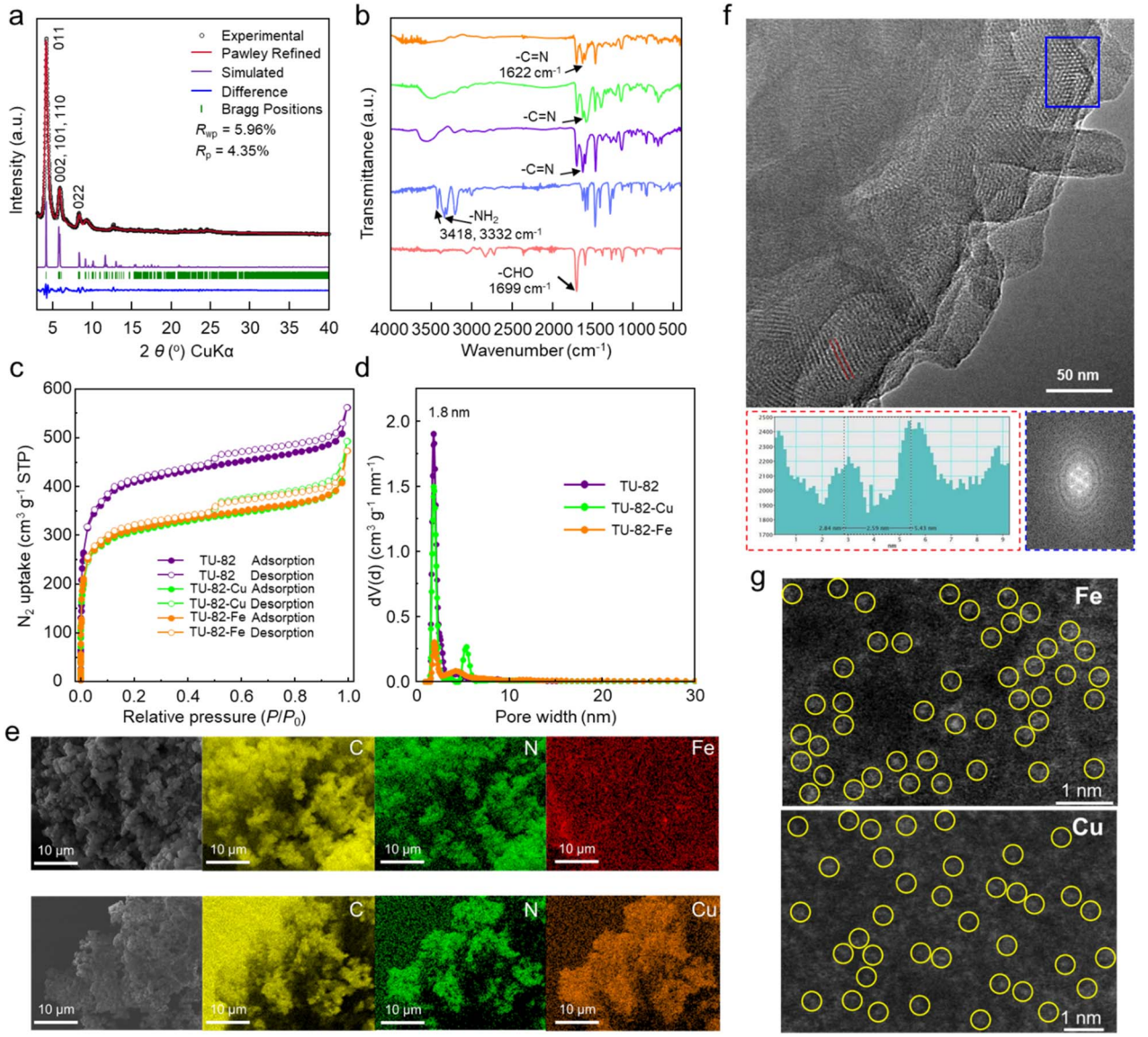

Fig. 2 (a) XRD patterns of TU-82. (b) FT-IR spectra of DPTB-Me (pink), Bpy (blue), TU-82 (purple), TU-82-Cu (green), and TU-82-Fe (orange). (c) N_2 adsorption–desorption isotherms of TU-82 and its metalated analogues. (d) Pore size distributions of TU-82, TU-82-Fe, and TU-82-Cu derived from QSDFT analysis using a cylindrical pore model. (e) SEM images and corresponding EDS elemental maps of TU-82-Fe (top) and TU-82-Cu (bottom), confirming uniform metal distribution. (f) HR-TEM image of TU-82 with FFT pattern from the blue-marked region and a distance–intensity profile from the red-marked section, revealing lattice fringes with a *d*-spacing of 2.59 nm. (g) HAADF-STEM images of TU-82-Fe (top) and TU-82-Cu (bottom), indicating atomic-level dispersion of metal centers.

models (Fig. 2a). Geometrical optimization was performed using the Forcite module in Materials Studio 7.0,(ref. 41) employing classical force-field-based methods. The refined structure revealed that TU-82 adopts a non-interpenetrated **bcu** topology (Fig. 1b), crystallizing in the orthorhombic space group *Imm*2 (No. 44), with unit cell parameters of $a = 17.4656$ Å, $b = 29.2450$ Å, and $c = 33.0385$ Å ($\alpha = \beta = \gamma = 90°$; Table S5). The experimental PXRD pattern exhibited distinct Bragg reflections at 2θ values of 4.14°, 5.84°, and 8.29°, which were indexed to the (011), a multiplet comprising the overlapping (002), (101), and (110) reflections, and the (022) crystallographic planes, respectively. Pawley refinement yielded excellent agreement between the experimental and simulated patterns, with low residuals ($R_p = 4.35\%$, $R_{wp} = 5.96\%$), confirming the structural fidelity of the proposed model. The close match between observed and calculated patterns, along with minimal deviation in the difference profile, underscores the long-range periodicity and high structural order of the synthesized TU-82 framework. Furthermore, the PXRD profiles of TU-82-M (M = Fe, Cu) exhibited identical peak positions to the pristine TU-82, confirming that the incorporation of metal ions did not disrupt the underlying framework integrity and that the crystallinity of the COF was fully retained post-metalation (Fig. S2).

The formation of the imine-linked framework in TU-82 was confirmed through a combination of Fourier-transform infrared (FT-IR) spectroscopy and solid-state ^{13}C cross-

polarization magic angle spinning (CP/MAS) NMR analysis. In the FT-IR spectrum of TU-82, a characteristic C=N stretching band appeared prominently at 1622 cm^{-1}, verifying the establishment of imine linkages. Concurrently, significant attenuation of the N–H stretching vibrations of the bipyridyl diamine monomer (originally at 3418 and 3332 cm^{-1}) and the aldehyde C=O band of DPTB-Me (at 1699 cm^{-1}) indicated complete consumption of the starting functional groups, supporting the successful progression of Schiff-base polymerization (Fig. 2b). Notably, TU-82-Fe and TU-82-Cu retained similar vibrational profiles in the FT-IR spectra, affirming that the framework's integrity was preserved following metal coordination. Complementary ^{13}C CP/MAS NMR spectroscopy further substantiated COF formation, with a distinct resonance at ~161 ppm attributed to the imine carbon (C=N) (Fig. S3). Elemental analysis of TU-82 ($C_{160}H_{100}N_{32}$) revealed measured values (C: 72.11; H: 4.27; N: 14.28) in close proximity to theoretical predictions (C: 77.80; H: 4.05; N: 18.15), validating the expected framework stoichiometry. Porosity and surface area properties of TU-82 and its metalated analogues were evaluated by nitrogen adsorption–desorption measurements at 77 K following thermal activation at 100 °C for 8 h. The nitrogen sorption isotherms of TU-82 exhibited a steep uptake at low relative pressures (P/P_0 < 0.1), indicative of intrinsic microporosity, along with a hysteresis loop at higher relative pressures, suggesting the presence of mesopores (Fig. 2c and S3). The Brunauer–Emmett–Teller (BET) surface area was determined to be 1527 $m^2\ g^{-1}$ based on multipoint fitting in the low-pressure region. Upon postsynthetic metalation, the resulting TU-82-Fe and TU-82-Cu frameworks maintained the porous nature of the parent COF, albeit with moderately reduced BET surface areas of 1168 and 1163 $m^2\ g^{-1}$, respectively. This reduction is ascribed to partial pore volume occupation and increased framework density due to coordinated metal ions. Quenched solid density functional theory (QSDFT) analysis employing a cylindrical pore model revealed a narrow pore size distribution centered at ~1.8 nm for all three materials (Fig. 2d), in excellent agreement with the structural model (Fig. S9). Importantly, the preservation of pore size and isotherm profile across TU-82, TU-82-Fe, and TU-82-Cu further corroborates that the metalation process did not compromise the intrinsic porosity or framework architecture.

Scanning electron microscopy (SEM) images revealed that TU-82 crystallizes into well-defined, isometric microcrystals with uniform morphology (Fig. S5). Upon postsynthetic metalation, SEM coupled with energy-dispersive X-ray spectroscopy (EDS) elemental mapping confirmed the successful incorporation and homogeneous spatial distribution of Fe and Cu within the TU-82-Fe and TU-82-Cu frameworks, respectively (Fig. 2e). The quantitative metal content was further determined by inductively coupled plasma mass spectrometry (ICP-MS), yielding average loadings of 6.42 wt% Fe and 8.95 wt% Cu across three independent measurements (Table S1), consistent with efficient coordination at bipyridyl sites. High-resolution transmission electron microscopy (HR-TEM) analysis provided further structural insights into the crystallinity of TU-82 (Fig. 2f and S6). Clear lattice fringes were observed with a *d*-spacing of 2.59 nm (Fig. 2f), which corresponds well to the (001) plane as predicted from the crystallographic model (Fig. 1b). We note that HRTEM probes only local ultrathin regions (<10 nm) and depends on specific domain orientations under the electron beam, which can enable the visualization of well-oriented (001) planes. In contrast, PXRD reflects the bulk-averaged structure, where (001) reflections of low abundance, weak crystallinity, or overlap with stronger peaks (*e.g.*, (100)/(110)) may render them less discernible in the diffraction pattern (Fig. 2a). Fast Fourier transform (FFT) analysis of the HR-TEM images further affirmed the long-range periodicity of the framework. High-angle annular dark-field scanning transmission electron microscopy (HAADF-STEM) images of TU-82-Fe and TU-82-Cu showed bright, atomically dispersed contrast features—attributable to the heavier Fe and Cu atoms—distributed uniformly throughout the framework (Fig. 2g). Although occasional larger bright spots and lighter contrast features are visible, these can be ascribed to overlapping atomic columns or local thickness variations of the COF matrix rather than metal aggregation, since no lattice fringes corresponding to metallic Fe or Cu nanocrystals were observed. Furthermore, X-ray photoelectron spectroscopy (XPS) and extended X-ray absorption fine structure (EXAFS) analyses revealed the metals to be present in well-defined coordination environments without signatures of metallic bonding or cluster formation (described later). These results confirm that the observed contrast originates from isolated Fe and Cu centers uniformly embedded within the COF lattice, thereby excluding the presence of aggregated nanoparticles and validating the single-site catalytic behavior of TU-82-Fe and TU-82-Cu. The thermal stability of the pristine and metalated frameworks was evaluated by thermogravimetric analysis (TGA) under nitrogen. TU-82 demonstrated excellent thermal robustness with negligible weight loss up to ~420 °C (Fig. S7), indicative of a thermally resilient network. The metalated analogues, while showing early-stage mass loss attributable to residual solvent and weakly coordinated species, retained appreciable stability under operating conditions. To evaluate the chemical robustness of the framework, TU-82 was immersed in a variety of protic and aprotic solvents relevant to NO_3RR electrochemistry. PXRD patterns collected after 24 h of solvent exposure confirmed that the framework crystallinity remained intact (Fig. S8), underscoring the high chemical stability of the COF scaffold.

To elucidate the electronic environment and coordination states of the metal centers in TU-82-Fe and TU-82-Cu, comprehensive XPS and X-ray absorption spectroscopy (XAS) analyses were conducted. The wide-scan XPS spectra confirmed the presence of C, N, and the respective metal species (Fe or Cu) in the frameworks (Fig. S10). High-resolution C 1s spectra of TU-82 and its metalated analogues displayed nearly identical peak profiles, indicating that the backbone structure of the COF remained chemically stable upon metal coordination (Fig. S11). The N 1s XPS spectrum of pristine TU-82 exhibited two distinct peaks at 398.5 eV and 400.9 eV, corresponding to pyridinic and imine nitrogen species, respectively (Fig. 3a).[36] Upon metalation, these binding energies shifted slightly due to coordination effects: TU-82-Fe showed peaks at 398.7 eV (pyridinic N)

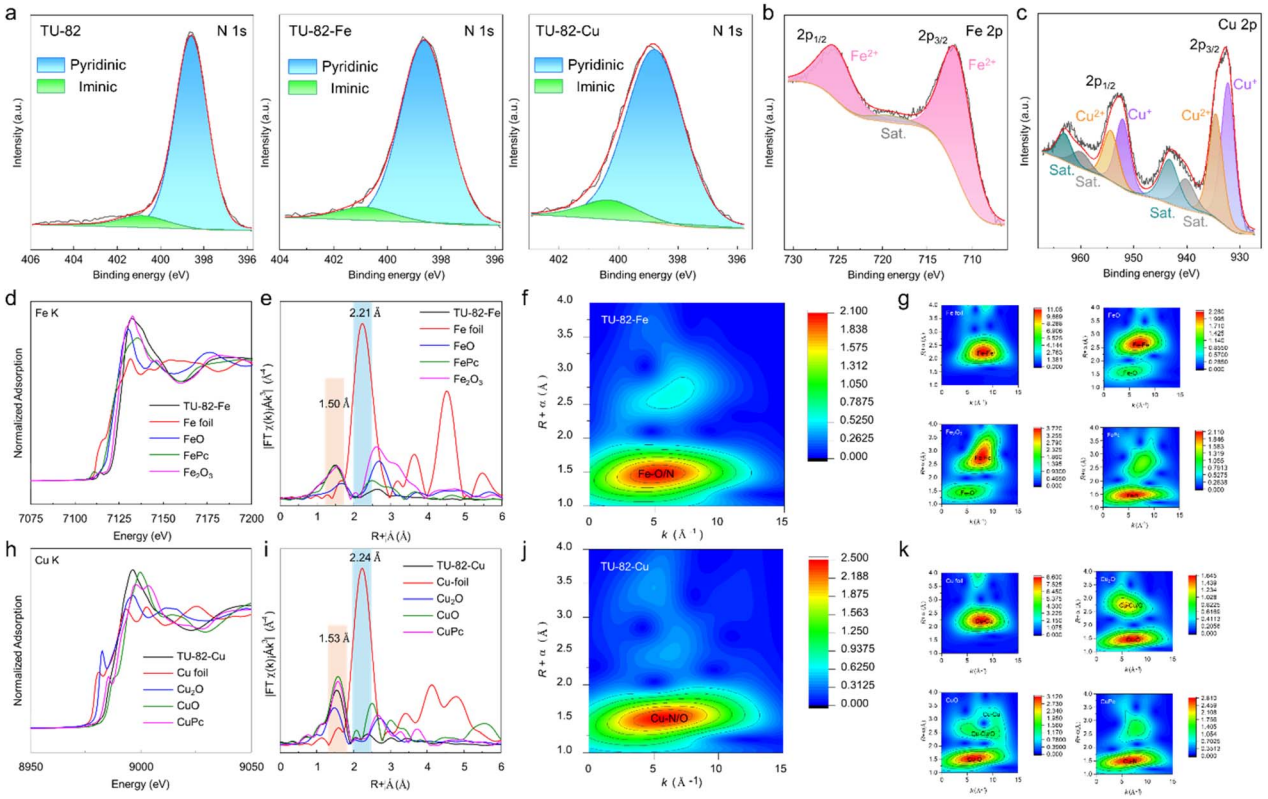

Fig. 3 (a) N 1s XPS spectra of TU-82, TU-82-Fe, and TU-82-Cu. (b) High-resolution Fe 2p XPS spectrum of TU-82-Fe. (c) High-resolution Cu 2p XPS spectrum of TU-82-Cu. (d) Fe K-edge XANES and (e) FT-EXAFS spectra of TU-82-Fe and reference materials (FePc, FeO, Fe_2O_3, and Fe foil; Pc: phthalocyanine). (f and g) WT-EXAFS plots for Fe in TU-82-Fe and reference compounds. (h) Cu K-edge XANES and (i) FT-EXAFS spectra of TU-82-Cu and reference compounds (CuPc, CuO, Cu_2O, and Cu foil). (j and k) WT-EXAFS plots for Cu in TU-82-Cu and reference compounds.

and 401.0 eV (imine N), while TU-82-Cu exhibited similar features at 398.8 eV and 400.4 eV, respectively, corroborating the formation of metal-nitrogen coordination bonds at the bipyridyl sites. Further insights into the oxidation state and coordination configuration were gained from the high-resolution Fe 2p and Cu 2p XPS spectra. For TU-82-Fe, two prominent peaks appeared at 712.1 eV (Fe $2p_{3/2}$) and 725.7 eV (Fe $2p_{1/2}$), indicative of Fe(II).[36] In the case of TU-82-Cu, characteristic Cu 2p peaks were observed at 932.2 eV and 952.2 eV, assigned to Cu(I), alongside additional signals at 934.5 eV and 954.3 eV corresponding to Cu(II), suggesting the coexistence of mixed valence states.[37,42,43] To further investigate the local coordination environment of the metal sites, X-ray absorption near-edge structure (XANES) and EXAFS analyses were performed. The Fe K-edge XANES spectrum of TU-82-Fe displayed an absorption edge beyond those of FeO and Fe_2O_3 (Fig. 3d). This coordination configuration of Fe atoms in TU-82-Fe was probed through EXAFS fitting of the Fe K-edge data that revealed a primary coordination number of 5.3 ± 0.3 (Table S2, Fig. S14), suggesting a five-coordinate geometry, likely comprising two nitrogen atoms from the bipyridine ligands and three oxygen atoms from acetate groups originating from the $Fe(OAc)_2$ precursor. This mixed N/O coordination geometry is analogous to previously reported structures such as BiPy-COF-Mn, which also featured five-coordinate metal centers. The Fourier-transformed (FT) EXAFS spectrum of TU-82-Fe exhibited a main peak at ~1.50 Å (phase uncorrected), attributed to Fe–N/O scattering, and the absence of a signal near 2.21 Å confirmed the lack of Fe–Fe bonds, ruling out the presence of Fe aggregates or nanoparticles (Fig. 3e). This was further corroborated by wavelet transform (WT) analysis of the EXAFS data, where the intensity maximum centered around 4.5 $Å^{-1}$ (in *k*-space) and 1.5 Å (in *R*-space) was characteristic of light atom scatterers (N or O), validating the isolated single-site nature of Fe centers (Fig. 3f and g). Analogous characterization of TU-82-Cu by Cu K-edge XANES placed the absorption edge between those of Cu_2O and CuO, and closer to CuO (Fig. 3h). This coordination state was understood through EXAFS fitting that revealed a Cu coordination number of 4.1 ± 0.2 (Table S2, Fig. S15), consistent with a square-planar or tetrahedral geometry involving bipyridine N-donors and acetate O-ligands. The FT-EXAFS spectrum of TU-82-Cu showed a prominent peak at ~1.53 Å, again attributable to Cu–N/O coordination, and lacked any significant signal near 2.24 Å, confirming the absence of Cu–Cu interactions (Fig. 3i). WT-EXAFS plots reinforced these findings, displaying intensity maxima characteristic of light-atom coordination environments (Fig. 3j and k). Together, these spectroscopic analyses definitively establish that both Fe and Cu centers in TU-82-M are atomically dispersed, occupy well-defined coordination environments involving bipyridine nitrogen and acetate oxygen ligands, and are free from metallic clustering. These structural attributes are critical to the

observed catalytic activity and selectivity in nitrate electroreduction.

To evaluate the electrocatalytic efficacy of TU-82-Fe and TU-82-Cu toward nitrate reduction to ammonia, a series of electrochemical measurements were performed in an H-type two-compartment cell. Each metalated COF was homogeneously mixed with carbon black and uniformly cast onto a 1×1 cm^2 carbon paper substrate, achieving a consistent catalyst loading of 0.4 mg cm^{-2}. All potentials were referenced to RHE. Linear sweep voltammetry (LSV) measurements carried out in an electrolyte solution of 0.1 M KNO_3 and 0.1 M KOH revealed distinct onset potentials and activity profiles for each catalyst (Fig. 4a). TU-82-Fe exhibited a significant increase in current density at approximately −0.21 V, while TU-82-Cu required a more negative onset of −0.23 V to elicit a comparable response, indicative of superior catalytic kinetics on the Fe site. TU-82-Fe consistently outperformed its Cu counterpart across the potential window, reaching a current density of 53 mA cm^{-2} at −0.80 V, compared to 43 mA cm^{-2} for TU-82-Cu. Chronoamperometric (i–t) measurements were employed to quantify the ammonia generated, using the indophenol blue method and UV-vis absorption at 654 nm (Fig. S16). As shown in Fig. 4b,

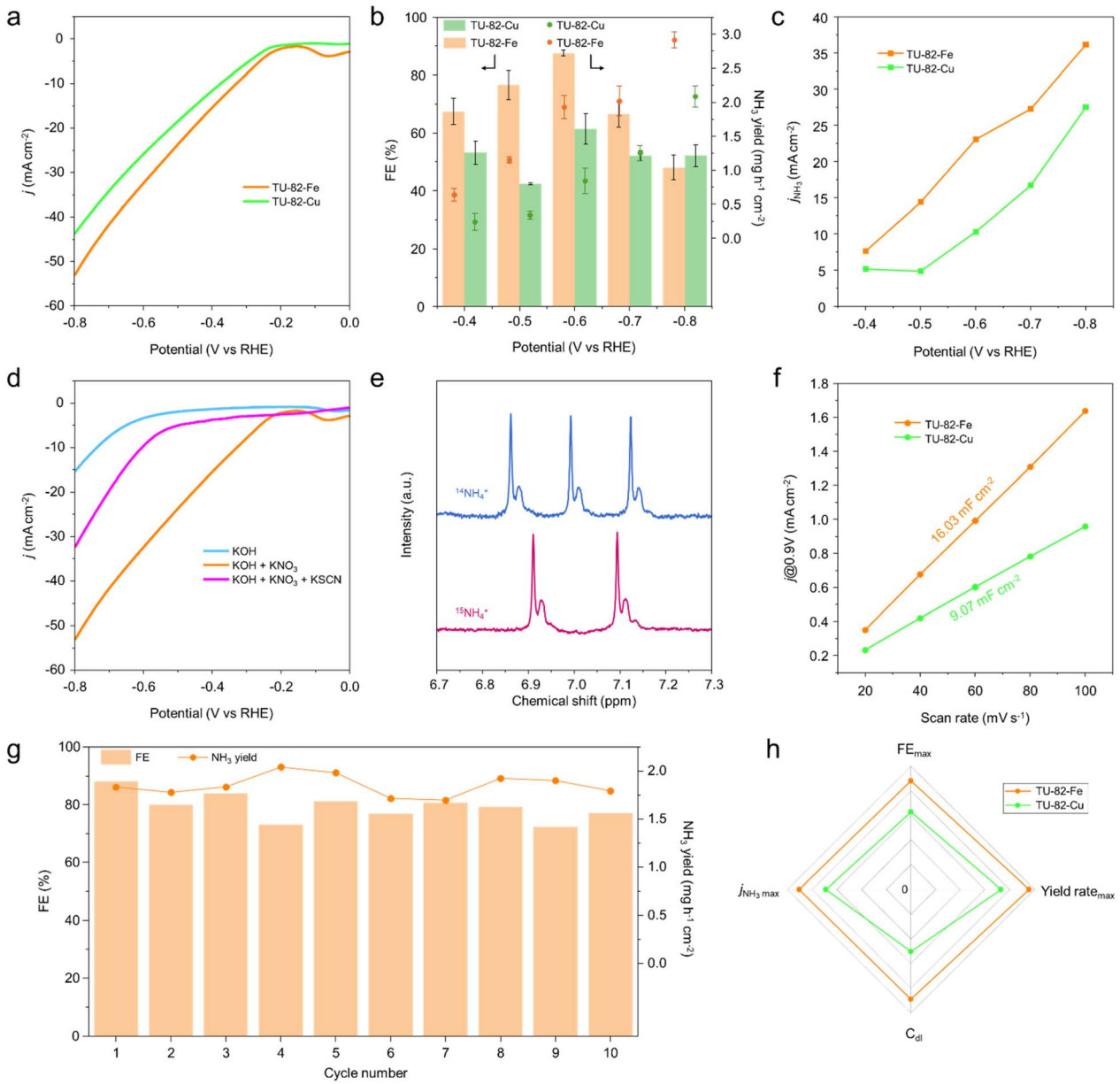

Fig. 4 (a) LSV curves of TU-82-Fe and TU-82-Cu recorded in 0.1 M KOH + 0.1 M KNO_3 mixed electrolyte. (b) FE and NH_3 yield rates as a function of applied potential. (c) NH_3 partial current densities (j_{NH3}) derived from FE and total current. (d) LSV responses of TU-82-Fe in 0.1 M KOH, 0.1 M KOH + 0.1 M KNO_3, and with the addition of 0.1 M KSCN to probe active site inhibition. (e) ^{1}H NMR spectra of NH_3 produced using $^{14}NO_3^-$ and $^{15}NO_3^-$ isotopes. (f) Electrochemical double-layer capacitance (C_{dl}) curves used to estimate ECSA. (g) Stability evaluation of TU-82-Fe over 10 electrolysis cycles at −0.6 V *vs.* RHE. (h) Radar chart comparison of TU-82-Fe and TU-82-Cu in terms of FE_{max}, maximum NH_3 yield rate, C_{dl}, and maximum j_{NH3}. Error bars in panel (b) represent the standard deviation from three independent measurements.

TU-82-Fe exhibited a volcano-type trend in FE with increasing overpotential, peaking at 88.1% at −0.60 V, while the yield rate increased monotonically, attaining 2.87 mg h^{-1} cm^{-2} at −0.80 V. In contrast, TU-82-Cu did not display a well-defined volcano profile. Instead, the FE fluctuated across the tested potentials, with a notably low efficiency of 42.5% at −0.50 V. This reduced selectivity may stem from heightened hydrogen evolution activity at this intermediate potential, which competes for protons and electrons, thereby diminishing nitrate-to-ammonia conversion. The highest FE achieved for TU-82-Cu was 62.8% at −0.60 V, accompanied by a yield rate of 2.19 mg h^{-1} cm^{-2} at −0.80 V. Partial current densities for NH_3 production, calculated from FE and total current density (Fig. 4c), further confirmed the superior performance of TU-82-Fe. At −0.80 V, TU-82-Fe achieved an NH_3 partial current density of 36.19 mA cm^{-2}, substantially surpassing that of TU-82-Cu (27.56 mA cm^{-2}). Byproduct formation was assessed using the Griess assay to quantify NO_2^- (Fig. S17). The results indicated trace NO_2^- generation over the entire potential range for TU-82-Fe, while TU-82-Cu exhibited comparatively higher NO_2^- formation (Fig. S18), further substantiating the higher selectivity of the Fe-based catalyst. To ensure comprehensive selectivity evaluation, gaseous byproducts were quantified using gas chromatography equipped with a thermal conductivity detector (GC-TCD) and calibration curves. Only trace amounts of N_2 (Fig. S19) and H_2 (Fig. S20) were detected across all applied potentials, confirming that TU-82-Fe effectively suppresses competing pathways and maintains high selectivity toward NH_3. Control experiments were designed to clarify the catalytic origin of the activity. LSV in 0.1 M KOH devoid of nitrate revealed a positive shift in the onset potential from −0.21 V to −0.65 V for TU-82-Fe, along with a sharp decline in current density (Fig. 4d). This confirms that the observed electrocatalytic response originates from NO_3^- reduction rather than competing hydrogen evolution. The introduction of 0.1 M KSCN, a strong chelator of single metal sites, led to pronounced suppression in current and a delayed onset potential (∼−0.57 V), underscoring the critical role of coordinated Fe centers in the bipyridyl motifs as the primary active sites.

To conclusively verify the nitrogen source in the reduced product, isotope-labeling experiments were conducted using $^{15}NO_3^-$ in place of $^{14}NO_3^-$. The resultant NH_3 was characterized by ^1H NMR spectroscopy (Fig. 4e). The spectrum of $^{14}NH_3$ displayed a triplet pattern with a ^1J (N–H) coupling constant of 52 Hz, characteristic of coupling with a spin-1 ^{14}N nucleus. In contrast, the spectrum of $^{15}NH_3$ exhibited a doublet pattern with a coupling constant of 72 Hz, consistent with spin-$\frac{1}{2}$ ^{15}N. This distinct shift in splitting patterns and coupling constants provides unambiguous evidence that the nitrogen in the NH_3 product originates exclusively from the nitrate feedstock, not from adventitious contamination. Electrochemical double-layer capacitance (C_{dl}), derived from cyclic voltammetry in the non-faradaic region (Fig. S21), was used as a proxy for electrochemical surface area (ECSA). TU-82-Fe exhibited a substantially higher C_{dl} (16.03 mF cm^{-2}) than TU-82-Cu (9.07 mF cm^{-2}), suggesting more abundant or accessible active sites, consistent with its higher NO_3RR performance (Fig. 4f). The operational durability of TU-82-Fe was assessed over 10 continuous electrolysis cycles at −0.60 V (Fig. 4g). The catalyst retained an average FE of ∼77.0% and an NH_3 yield of ∼1.79 mg h^{-1} cm^{-2}, demonstrating excellent long-term stability and resilience under operating conditions. To assess industrial relevance, chronopotentiometric measurements were carried out at a high current density of 120 mA cm^{-2}, where TU-82-Fe displays a stable potential profile under sustained NO_3RR operation (Fig. S22). Furthermore, long-term electrolysis over 100 h at −0.6 V *vs.* RHE reveals consistent catalytic performance (Fig. S23), demonstrating excellent durability beyond the initial cycling tests. The catalytic activity of TU-82-Fe was further examined across a wide pH range (1–13) to assess its robustness under conditions relevant to real wastewater. As shown in Fig. S24, the catalyst remains active under acidic and neutral conditions and achieves its highest FE and NH_3 yield in alkaline media, demonstrating broad pH tolerance and strong operational versatility. XRD and FT-IR analyses (Fig. S25) confirmed that the material retained its crystallinity and chemical integrity after cycling tests, indicating excellent structural stability. Post-NO_3RR XPS analysis confirms that the bipyridine-Fe coordination environment in TU-82-Fe remains fully preserved after electrolysis. The N 1s (Fig. S26a) and Fe 2p (Fig. S26b) spectra showed negligible shifts in binding energies and retention of the Fe(II) oxidation state, demonstrating that neither ligand degradation nor metal demetalation occured during catalysis. A radar chart summarizing and comparing key performance metrics—FE, yield rate, NH_3 partial current density, and C_{dl}—for TU-82-Fe and TU-82-Cu (Fig. 4h) clearly highlights the superior electrochemical behavior of the Fe-based catalyst. Notably, TU-82-Fe exhibits performance benchmarks that rival or exceed those of leading state-of-the-art NO_3RR catalysts (Table S3), underscoring its promise for practical and scalable ammonia electrosynthesis.

To elucidate the structure–activity relationship of TU-82-M in electrocatalytic NO_3RR, density functional theory (DFT) calculations were performed. Four possible mechanistic pathways were constructed, each describing the transformation of NO_3^- to NH_3 *via* a series of adsorbed intermediates. The free energy diagrams for TU-82-Fe and TU-82-Cu (Fig. 5a and Table 1) reveal that the key divergence between pathways lies in the NO* to NH_2^* transformation, where two main routes involving either NOH* (Path 1, dotted lines) or NHO* (Path 2, solid lines) intermediates are energetically feasible. For TU-82-Fe, the activation energy for the NO* → NHO* step is significantly lower (0.354 eV) than that for NO* → NOH* (1.131 eV), indicating that the reaction preferentially proceeds *via* the NHO-mediated pathway. A similar trend is observed for TU-82-Cu, where the NO* → NHO* step requires 0.814 eV, while NO* → NOH* is substantially less favorable (1.531 eV). These findings suggest that both catalytic sites favor the NHO* intermediate pathway, wherein NHO* is sequentially hydrogenated to NHOH*, followed by protonation to NH_2OH*, which undergoes dehydration to form NH_2^*. The final protonation yields NH_3. Moreover, the lower energy barrier for the rate-determining NO* → NHO* step on TU-82-Fe rationalizes its superior experimental NO_3RR performance relative to TU-82-Cu. Notably, the TU-82-Fe site offers

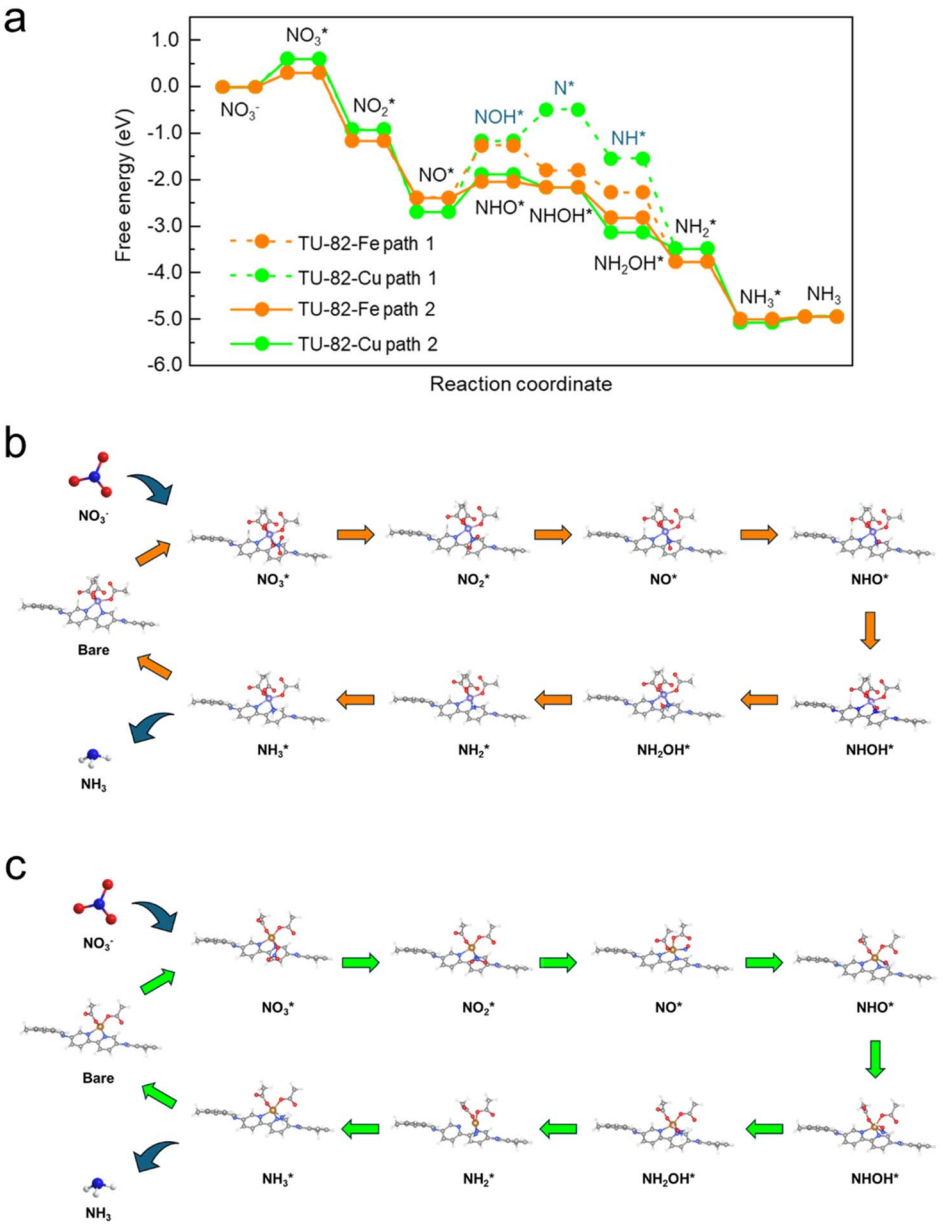

Fig. 5 (a) Calculated free energy profiles for NO_3RR on TU-82-Fe and TU-82-Cu, highlighting the divergence in energetics for the NO* to NH_2^* step *via* two plausible pathways involving NOH* (Path 1, dotted lines) and NHO* (Path 2, solid lines) intermediates. (b and c) optimized adsorption configurations of key NO_3RR intermediates on TU-82-Fe and TU-82-Cu, showing metal–adsorbate interactions at the bipyridyl-coordinated metal sites.

a more favorable energy landscape throughout the entire reaction coordinate, reinforcing its catalytic advantage. The complete reaction pathway, consistent with both theoretical predictions and experimental product distribution, is proposed as: $NH_3^- \rightarrow NO_3^* \rightarrow NO_2^* \rightarrow NO^* \rightarrow NHO^* \rightarrow NHOH^* \rightarrow NH_2OH^* \rightarrow NH_2^* \rightarrow NH_3^* \rightarrow NH_3$ (Fig. 1d). This mechanism also explains the detection of NO_2^- as a main byproduct, attributable to the facile desorption of NO_2^* from the catalytic surface. The most stable adsorption configurations of each intermediate on TU-82-Fe and TU-82-Cu were fully optimized (Fig. 5b and c), revealing strong metal-adsorbate interactions at the bipyridyl-coordinated metal centers. These configurations reflect the geometric adaptability of the 3D COF scaffold, which offers a well-defined coordination environment that supports stable binding and transformation of reactive intermediates. A complete thermodynamic profile including electronic energies (E), zero-point energy corrections (ZPE), entropic contributions (T.S), and Gibbs free energies ($G = E + ZPE - T S$) of each intermediate is summarized in Table S4. These data provide quantitative support for the proposed reaction mechanism and further validate the superior kinetic and thermodynamic profile of TU-82-Fe. Overall, the DFT results highlight the critical role of metal identity in determining the reaction pathway and kinetics and underscore the structural advantages of TU-82's 3D framework in supporting active, isolated metal sites. This study offers a compelling demonstration of how topologically

Table 1 Calculated Gibbs free energy changes (ΔG, in eV) for the proposed NO_3RR pathways on TU-82-Fe and TU-82-Cu catalysts, derived from DFT calculations. Path 1 proceeds *via* NOH intermediates, while Path 2 follows the NHO* route. Energetics are given for each elementary step from NO_3^- to NH_3 through adsorbed intermediates*

	TU-82-Cu	TU-82-Fe
Path 1		
$NO_3^- \rightarrow NO_3^*$	0.605	0.307
$NO_3^* + 2(H^+ + e^-) \rightarrow NO_2^* + H_2O$	−1.517	−1.457
$NO_2^* + 2(H^+ + e^-) \rightarrow NO^* + H_2O$	−1.773	−1.231
$NO^* + (H^+ + e^-) \rightarrow NOH^*$	**1.531**	**1.131**
$NOH^* + (H^+ + e^-) \rightarrow N^* + H_2O$	0.673	−0.535
$N^* + (H^+ + e^-) \rightarrow NH^*$	−1.054	−0.479
$NH^* + (H^+ + e^-) \rightarrow NH_2^*$	−1.947	−1.495
$NH_2^* + (H^+ + e^-) \rightarrow NH_3^*$	−1.581	−1.229
$NH_3^* \rightarrow NH_3$	0.135	0.062
Path 2		
$NO_3^- \rightarrow NO_3^*$	0.605	0.307
$NO_3^* + 2(H^+ + e^-) \rightarrow NO_2^* + H_2O$	−1.517	−1.457
$NO_2^* + 2(H^+ + e^-) \rightarrow NO^* + H_2O$	−1.773	−1.231
$NO^* + (H^+ + e^-) \rightarrow NHO^*$	**0.814**	**0.354**
$NHO^* + (H^+ + e^-) \rightarrow NHOH^*$	−0.287	−0.120
$NHOH^* + (H^+ + e^-) \rightarrow NH_2OH^*$	−0.968	−0.662
$NH_2OH^* + (H^+ + e^-) \rightarrow NH_2^* + H_2O$	−0.355	−0.951
$NH_2^* + (H^+ + e^-) \rightarrow NH_3^*$	−1.581	−1.229
$NH_3^* \rightarrow NH_3$	0.135	0.062

sophisticated COF platforms can be tailored to promote selective and efficient nitrogen-cycle electrocatalysis.

3. Conclusions

This work presents a transformative advancement in the development of COF-based electrocatalysts by introducing TU-82, a novel 3D COF platform applied to the electrochemical NO_3RR. Unlike conventional 2D COF systems, TU-82 leverages a high-connectivity [8 + 2] topology and a rigid **bcu** network derived from rational topological design using an octatopic tetragonal prismatic node and a linear bipyridyl linker. This deliberate architectural strategy enables spatially precise metalation of bipyridyl coordination sites, thereby establishing uniformly distributed, catalytically active Fe and Cu centers within a robust and porous 3D scaffold. The superior performance of TU-82-Fe in NO_3RR—evidenced by its high FE (88.1% at −0.6 V *vs.* RHE), notable ammonia yield (2.87 mg h^{-1} cm^{-2} at −0.8 V *vs.* RHE), and long-term durability—demonstrates the power of 3D framework engineering in tuning electrocatalytic function. Theoretical calculations corroborate these findings, revealing that Fe sites within the TU-82 scaffold facilitate a more energetically favorable NHO-mediated reaction pathway, with a notably low barrier for the rate-determining NO* → NHO* step. More broadly, this contribution establishes a conceptual and structural foundation for expanding the application of 3D COFs in electrocatalysis. By demonstrating how deliberate lattice design and coordination site engineering in 3D frameworks can drive selective multi-electron transformations, this work paves the way for the development of next-generation porous materials tailored for sustainable nitrogen conversion, clean energy processes, and programmable catalytic systems.

4. Experimental section

4.1. Synthesis of TU-82

A finely ground mixture of DPTB-Me (19.04 mg, 0.03 mmol) and Bpy (22.35 mg, 0.12 mmol) was introduced into a Pyrex tube (ID: 8 mm; OD: 10 mm). To the mixture was added 0.25 mL of *o*-dichlorobenzene and 0.75 mL of *n*-butanol. Following 10 min of sonication, 0.2 mL of 6 M aqueous acetic acid was added dropwise. The resulting mixture was sonicated for an additional 10 min to ensure a homogenous suspension. The tube was flash-frozen in liquid nitrogen (77 K), degassed by three freeze–pump–thaw cycles, flame-sealed under vacuum, and heated at 120 °C for 72 h. Upon cooling to room temperature, the resulting solid was isolated *via* centrifugation, washed with THF (5 × 10 mL), Soxhlet extracted in THF for 24 h, and dried *in vacuo* at 100 °C for 12 h to afford TU-82 as a yellow powder (73% yield). Anal. Calcd. for $C_{160}H_{100}N_{32}$: C: 77.80; H: 4.05; N: 18.15. Found: C: 72.11; H: 4.27; N: 14.28.

4.2. Preparation of TU-82-M (M = Fe, Cu)

To prepare the metalated COF, TU-82 (40 mg) and the corresponding metal acetate salt ($Fe(OAc)_2$ or $Cu(OAc)_2$, 20 mg) were dispersed in methanol (40 mL) and stirred under reflux at 60 °C for 12 h under a continuous flow of argon. After completion, the resulting solid was collected by filtration, washed with methanol, and dried overnight in a desiccator under reduced pressure. For TU-82-Fe, the dried solid was further subjected to thermal treatment under a hydrogen atmosphere at 200 °C for 1 h, affording TU-82-Fe as a dark orange powder. For TU-82-Cu, the solid was thermally treated under vacuum at 100 °C for 4 h to yield TU-82-Cu as a dark green powder.

4.3. Preparation of catalyst slurry

To prepare the catalyst slurry, TU-82-M (3.75 mg) and carbon black (3.75 mg) were dispersed in a mixed solvent consisting of 2-propanol (1.27 mL), ultrapure water (215 μL), and 5 wt% Nafion™ dispersion (15 μL). The mixture was sonicated for 30 min to ensure homogeneous dispersion of the COF catalyst and carbon black (denoted as TU-82-M/CB), forming a uniform catalyst ink. Carbon black was introduced as a conductive additive to improve the electron transport within the catalyst layer and to ensure uniform dispersion of the COF on the electrode surface. The 1 : 1 mass ratio of TU-82-M to carbon black was chosen to balance electrical conductivity and active site exposure, a ratio that has also been employed in previous studies on COF-based electrocatalysts for nitrate reduction.[44] Therefore, the prepared catalyst slurry is denoted as TU-82-M/CB, highlighting that carbon black serves as a conductivity enhancer and dispersant rather than an independent catalytic phase.

4.4. Electrochemical measurements

All electrochemical measurements for nitrate reduction (NO_3RR) were carried out using an ECstat-302 electrochemical

workstation (EC FRONTIER, Japan) in a two-compartment H-type cell (EC FRONTIER, Japan) separated by an AMVN membrane. The working electrode was prepared by drop-casting 16 μL aliquots of the catalyst slurry onto a 1 cm × 1 cm piece of carbon paper (SIGRACET®GDL 22BB), followed by drying at room temperature. This process was repeated 10 times to ensure sufficient catalyst loading. A platinum coil served as the counter electrode, and a silver/silver chloride (Ag/AgCl) electrode was used as the reference electrode. All potentials reported herein were converted to the reversible hydrogen electrode (RHE) scale using the equation:[45]

$$E_{RHE} = E_{Ag/AgCl} + 0.0591 \times pH + 0.1976$$

The electrolyte in both chambers consisted of 0.1 M KNO_3 and 0.1 M KOH (pH ≈ 13). Prior to each electrolysis, the electrolyte was purged with Ar gas for 20 min. Chronoamperometry (CA) was then conducted at the desired potential for 60 min. After each electrolysis cycle, the electrolyte was replaced with fresh solution before performing the next experiment.

4.4.1. Quantification of ammonia. The concentration of ammonia (NH_3) in the electrolyte after electrolysis was determined using the indophenol blue method. Post-electrolysis samples were first diluted with 0.1 M KNO_3 + 0.1 M KOH to ensure the NH_3 concentration fell within the linear detection range. To 2 mL of the diluted sample, 2 mL of a 1 M NaOH solution containing 5 wt% salicylic acid and 5 wt% sodium citrate, 1 mL of 0.05 M NaClO, and 0.2 mL of a 1 wt% $C_5FeN_6Na_2O$ solution were sequentially added. The resulting mixture was incubated at room temperature for 1 h. The absorbance of the formed indophenol blue complex was measured at 654 nm using a UV-visible spectrophotometer. A calibration curve was generated by plotting absorbance at 654 nm against standard NH_3 solutions (0, 0.5, 1.0, 2.0, 3.0, 4.0, 5.0 ppm), and used to quantify the ammonia concentration in each sample.

4.4.2. Isotope labelling experiments. To confirm that the ammonia detected during electrocatalytic NO_3RR originated exclusively from the nitrate reactant, isotope labelling experiments were performed using $K^{15}NO_3$ (98 atom% ^{15}N, Sigma-Aldrich). The electrolyte consisted of 0.1 M $K^{15}NO_3$ and 0.1 M KOH (pH ≈ 13). Prior to electrolysis, the electrolyte was purged with Ar gas for 20 min to eliminate dissolved oxygen and minimize interference from atmospheric nitrogen species. CA was carried out at −0.6 V *vs.* RHE for 60 min, following the same procedure described previously. After electrolysis, 600 μL of the electrolyte was collected and mixed with 100 μL of 1 M HCl(aq) and 100 μL of D_2O for nuclear magnetic resonance (NMR) analysis. The resulting ammonia was analyzed by proton nuclear magnetic resonance spectroscopy (^1H NMR, Bruker Avance III 400 MHz NMR spectrometer). The use of D_2O served to suppress background proton signals and enabled field locking for accurate spectral acquisition. For comparison, a parallel control experiment was conducted using 0.1 M $K^{14}NO_3$ under otherwise identical conditions. This control supports that the observed $^{15}NH_3$ product ($^{15}NH_4^+$) in the labelled experiment originated directly from the electrochemical reduction of $^{15}NO_3^-$.

4.4.3. Quantification of nitrite. The concentration of nitrite (NO_2^-) was evaluated using the Griess assay. Electrolyte samples were diluted as needed to fall within the linear range of the method. The pH of each diluted sample was adjusted by adding 2.0 mL of 0.1 M HCl. The Griess reagent was freshly prepared by mixing 4 g of sulfanilamide, 0.2 g of *N*-(1-naphthyl) ethylenediamine dihydrochloride, 50 mL of ultrapure water (18 MΩ), and 10 mL of phosphoric acid. A 100 μL aliquot of this reagent was then added to the diluted electrolyte and incubated at room temperature for 10 min. The resulting azo dye complex was quantified by measuring the absorbance at 539 nm using UV–vis spectroscopy. Calibration was performed using NO_2^- standard solutions (0, 1.0, 2.0, 3.0, 4.0, 5.0 ppm).

4.4.4. Calculation of faradaic efficiency and yield.[46] The faradaic efficiencies for ammonia and nitrite production ($FENH_3$ and $FENO_2^-$) were calculated as the ratio of the charge associated with product formation to the total charge passed during electrolysis, according to the following expression:

$$FE = \frac{n \times F \times C \times V}{Q_{tot}} \times 100\%$$

where n is the number of electrons transferred per molecule of product (8 for NH_3, 2 for NO_2^-), F is the Faraday constant (96,485 C mol^{-1}), C is the concentration of product (mol L^{-1}), V is the volume of electrolyte (L), and Q_{tot} is the total charge passed, determined by integrating the current over the electrolysis time.

The NH_3 and NO_2^- yields are calculated according to the following equation:

$$Yield = \frac{C \times V}{A \times t}$$

where A is area of electrode (cm^2), and t is electrolysis time.

4.4.5. Electrochemical surface area (ECSA) analysis.[46] CV was conducted in the non-faradaic potential region at scan rates ranging from 20 to 100 mV s^{-1} to estimate the electrochemically active surface area. At each scan rate, the capacitive current was determined by averaging the absolute values of the anodic and cathodic currents (*i.e.*, $(|Ia| + |Ic|)/2$) at a fixed potential. A linear plot of the average current density *versus* scan rate was constructed, and the slope was taken as the electrochemical double-layer capacitance (C_{dl}). The ECSA was then calculated using the relation:

$$ECSA = C_{dl}/C_s$$

where C_s is the specific capacitance of a flat surface of the material, typically assumed to be 40 μF cm^{-2} for carbon-based electrodes.

4.4.6. Calculation of turnover frequency (TOF).[44]

$$\text{Turnover number (TON)} = \frac{NH_3 \text{ yield(mg)}}{\text{Catalyst loading(mg)}}$$

$$TOF = \frac{TON}{Time(h)}$$

4.5. Computational method

All density functional theory (DFT) calculations were performed using the Vienna *Ab initio* Simulation Package (VASP),[47,48] adopting the generalized gradient approximation (GGA) with the Perdew–Burke–Ernzerhof (PBE)[49] functional. The projected augmented wave (PAW)[50,51] potentials were utilized to describe the ionic cores and take valence electrons into account using a plane wave basis set with a kinetic energy cutoff of 450 eV. The DFT-D3 empirical correction method was used to account for the van der Waals interactions. Geometry optimizations were carried out with the force convergency smaller than 0.02 eV $Å^{-1}$.

To simulate the local environment of the catalytic site, a cluster model was extracted from the fully optimized 3D COF crystal structure. The terminal carbon atoms were saturated with hydrogen atoms. The terminal C–H bonds were optimized with all hydrogen atoms relaxed, while the rest of the cluster framework atoms were kept fixed. For adsorption calculations, the terminal atoms (including C atoms saturated by H and a complete benzene ring) were fixed, while the remaining framework atoms and adsorbates were allowed to relax. The COF fragment was placed in an orthorhombic simulation box of dimensions 20 Å × 20 Å × 30 Å. A $(1 \times 1 \times 1)$ *k*-point sampling with the gamma-centered scheme was employed for the Brillouin zone integration.

The free energy changes (ΔG) for each elementary step of the nitrate reduction reaction (NO_3RR) were calculated using the computational hydrogen electrode (CHE) model. This model assumes that the chemical potential of an electron–proton pair is equal to that of $\frac{1}{2}$ H_2 in the gas phase. The free energies of adsorption are then calculated by the following equation:

$$\Delta G = \Delta E + \Delta E_{ZPE} - T\Delta S$$

where ΔE, ΔE_{ZPE} and ΔS denote the changes of DFT energy, zero-point energy, and entropy, respectively.

The adsorption free energy of NO_3^-, denoted as G_{ad} (NO_3^-), was determined according to Fig. S1.[52,53] ΔG_1 corresponds to the reaction free energy from gas HNO_3(g) to adsorbed NO_3^* and (H^+ + e^-), and can be evaluated based on the CHE model. The free energy change from HNO_3(l) to HNO_3(g) was computed based on the difference in standard Gibbs free energy of formation between HNO_3 in liquid and gas, which is 0.075 eV. The formation of HNO_3(l) from NO_3^- in an aqueous solution is associated with a Gibbs free energy of 0.317 eV. All Gibbs free energy values were sourced from the CRC Handbook of Chemistry and Physics.[54] The final adsorption free energy is then expressed as:

$$G_{ad}(NO_3^-) = \Delta G_1 + 0.075 + 0.317$$

Author contributions

Y. Z. S. D and Y. N. conceived the study and supervised the project. T. I carried out the synthesis, characterization and application with assistance from A. K. K. S. K. S and M. N. S. T. K. S. and T. K. contributed to the NO_3RR experiments. S. D drafted the manuscript. All authors discussed the results and approved the final version of the manuscript.

Conflicts of interest

There are no conflicts to declare.

Data availability

The data supporting the findings of this study are provided in the main text and supplementary information (SI). Additional data are available from the corresponding author upon reasonable request. Supplementary information: materials and methods, PXRD of metalated COFs, solid-state ^{13}C CP-MAS NMR spectroscopy, BET surface area plot, SEM and TEM characterization, ICP-MS, TGA, chemical stability analysis, simulated structural model of TU-82, XPS, XANES analysis results, EXAFS fitting analysis results, electrochemical measurements, DFT calculations, and unit cell information and fractional atomic coordinates. See DOI: https://doi.org/10.1039/d5ta07989f.

Acknowledgements

This study was supported by the Scientific Research on Innovative Areas "Aquatic Functional Materials" (grant no. 22H04562), JSPS KAKENHI (grant no. 23H00289 and 23KK0098), the Yazaki Memorial Foundation for Science and Technology, and the FUSO Innovative Technology Fund.

Notes and references

1 L. Zhai, S. Liu and Z. Xiang, *Ind. Chem. Mater.*, 2023, **1**, 332–342.
2 J. Lim, C. A. Fernández, S. W. Lee and M. C. Hatzell, *ACS Energy Lett.*, 2021, **6**, 3676–3685.
3 W. I. F. David, G. D. Agnew, R. Bañares-Alcántara, J. Barth, J. B. Hansen, P. Bréquigny, M. de Joannon, S. Fürstenberg Stott, C. Fürstenberg Stott, A. Guati-Rojo, M. Hatzell, D. R. MacFarlane, J. W. Makepeace, E. Mastorakos, F. Mauss, A. Medford, C. Mounaïm-Rousselle, D. A. Nowicki, M. A. Picciani, R. S. Postma, K. H. R. Rouwenhorst, P. Sabia, N. Salmon, A. N. Simonov, C. Smith, L. Torrente-Murciano and A. Valera-Medina, *J. Phys. Energy*, 2024, **6**, 021501.
4 W. Song, L. Yue, X. Fan, Y. Luo, B. Ying, S. Sun, D. Zheng, Q. Liu, M. S. Hamdy and X. Sun, *Inorg. Chem. Front.*, 2023, **10**, 3489–3514.
5 W. Chen, X. Yang, Z. Chen, Z. Ou, J. Hu, Y. Xu, Y. Li, X. Ren, S. Ye, J. Qiu, J. Liu and Q. Zhang, *Adv. Funct. Mater.*, 2023, **33**, 2300512.
6 G.-F. Chen, Y. Yuan, H. Jiang, S.-Y. Ren, L.-X. Ding, L. Ma, T. Wu, J. Lu and H. Wang, *Nat. Energy*, 2020, **5**, 605–613.
7 Z. Qu, J. Hong, Y. Gao, J. Sun, J. Huang, M. Zhang, M. Zhu, T. Li, X. Wang, D. Gan, Q. Song, T. Zhang, R. Zhou, D. Liu, P. J. Cullen and R. Zhou, *Adv. Sci.*, 2025, **12**, 2411783.
8 W. Qiu, Y. Liu, M. Xie, Z. Jin, P. Li and G. Yu, *EES Catal.*, 2024, **2**, 202–219.

9 Z. Wang, D. Richards and N. Singh, *Catal. Sci. Technol.*, 2021, **11**, 705–725.
10 C. Wu, Y. Shen, L. Lv, X. Meng, X. Yang, X. Wang, X. Jiang, Q. Ai, Y. Shuai and Z. Zhou, *J. Mater. Chem. A*, 2025, **13**, 6631–6643.
11 R. Zhang, X. Ma, S. Zhang, Q. Li, Y. Zhao and C. Zhi, *ChemElectroChem*, 2025, **12**, e202400499.
12 L. Sun, H. Yao, F. Jia, Y. Wang and B. Liu, *Adv. Energy Mater.*, 2023, **13**, 2302274.
13 D. K. K. Kori and A. K. Das, *ACS Appl. Eng. Mater.*, 2023, **1**, 2386–2396.
14 R. Jia, Y. Wang, C. Wang, Y. Ling, Y. Yu and B. Zhang, *ACS Catal.*, 2020, **10**, 3533–3540.
15 S. Tomihari, M. Kamiyama, H. Minhas, T. Kawawaki, K. Takemae, Y. Shingyouchi, Z. Chen, B. Pathak and Y. Negishi, *ACS Catal.*, 2025, **15**, 20853–20863.
16 Z.-Y. Wu, M. Karamad, X. Yong, Q. Huang, D. A. Cullen, P. Zhu, C. Xia, Q. Xiao, M. Shakouri, F.-Y. Chen, J. Y. Kim, Y. Xia, K. Heck, Y. Hu, M. S. Wong, Q. Li, I. Gates, S. Siahrostami and H. Wang, *Nat. Commun.*, 2021, **12**, 2870.
17 L. Xie, Y. Wang, Q. Kong and R. Cao, *ChemCatChem*, 2024, **16**, e202400956.
18 O. M. Yaghi, M. J. Kalmutzki and C. S. Diercks, *Introduction to Reticular Chemistry: Metal–Organic Frameworks and Covalent Organic Frameworks, Wiley-VCH*, Weinheim, Germany, 2019, ch. 7–11, pp. 177–283.
19 T. Irie, S. Das, Q. Fang and Y. Negishi, *J. Am. Chem. Soc.*, 2025, **147**, 1367–1380.
20 K. T. Tan, S. Ghosh, Z. Wang, F. Wen, D. Rodríguez-San-Miguel, J. Feng, N. Huang, W. Wang, F. Zamora, X. Feng, A. Thomas and D. Jiang, *Nat. Rev. Methods Primers*, 2023, **3**, 1.
21 F. Haase and B. V. Lotsch, *Chem. Soc. Rev.*, 2020, **49**, 8469–8500.
22 S.-Y. Ding and W. Wang, *Chem. Soc. Rev.*, 2013, **42**, 548–568.
23 D. Blätte, F. Ortmann and T. Bein, *J. Am. Chem. Soc.*, 2024, **146**, 32161–32205.
24 S. Kandambeth, K. Dey and R. Banerjee, *J. Am. Chem. Soc.*, 2019, **141**, 1807–1822.
25 X. Zhao, P. Pachfule and A. Thomas, *Chem. Soc. Rev.*, 2021, **50**, 6871–6913.
26 Y. Song, Q. Sun, B. Aguila and S. Ma, *Adv. Sci.*, 2019, **6**, 1801410.
27 X. Han, C. Yuan, B. Hou, L. Liu, H. Li, Y. Liu and Y. Cui, *Chem. Soc. Rev.*, 2020, **49**, 6248–6272.
28 Y. Li, W. Chen, G. Xing, D. Jiang and L. Chen, *Chem. Soc. Rev.*, 2020, **49**, 2852–2868.
29 X. Li, P. Yadav and K. P. Loh, *Chem. Soc. Rev.*, 2020, **49**, 4835–4866.
30 C. Qian, L. Feng, W. L. Teo, J. Liu, W. Zhou and Y. Zhao, *Nat. Rev. Chem.*, 2022, **6**, 881–898.
31 J. Á. Martín-Illán, D. Rodríguez-San-Miguel and F. Zamora, *Coord. Chem. Rev.*, 2023, **495**, 215342.
32 S. Lin, C. S. Diercks, Y.-B. Zhang, N. Kornienko, E. M. Nichols, Y. Zhao, A. R. Paris, D. Kim, P. Yang, O. M. Yaghi and C. J. Chang, *Science*, 2015, **349**, 1208–1213.
33 H. Hu, R. Miao, F. Yang, F. Duan, H. Zhu, Y. Hu, M. Du and S. Lu, *Adv. Energy Mater.*, 2024, **14**, 2302608.
34 F. Lv, M. Sun, Y. Hu, J. Xu, W. Huang, N. Han, B. Huang and Y. Li, *Energy Environ. Sci.*, 2023, **16**, 201–209.
35 S. I. G. P. Mohamed, S. Namvar, T. Zhang, H. Shahbazi, Z. Jiang, A. M. Rappe, A. Salehi-Khojin and S. Nejati, *Adv. Mater.*, 2024, **36**, 2309302.
36 S. Lu, F. Yang, H. Hu, D. Li, H. Hu, J. Wang and M. Du, *J. Mater. Chem. A*, 2025, **13**, 9265–9273.
37 Y. Zhu, H. Duan, C. G. Gruber, W. Qu, H. Zhang, Z. Wang, J. Zhong, X. Zhang, L. Han, D. Cheng, D. D. Medina, E. Cortés and D. Zhang, *Angew. Chem., Int. Ed.*, 2025, **64**, e202421821.
38 J. Zhou, J. Zhao, D. Song, J. Liu, W. Xu, J. Li and N. Wang, *Inorg. Chem.*, 2024, **63**, 15177–15185.
39 M. Teng, J. Yuan, Y. Li, C. Shi, Z. Xu, C. Ma, L. Yang, C. Zhang, J. Gao and Y. Li, *J. Colloid Interface Sci.*, 2024, **654**, 348–355.
40 S. Yang, S. Bi, L. Zhai and Q. Xu, *Chem. Sci.*, 2025, **16**, 15611–15619.
41 *Materials Studio, Ver. 7.0*, Accelrys Inc., San Diego, CA, 2013.
42 X. Zhao, J. Chen, X. Mao, C. Li, L. He, F. Zhang, M. Zhang, J. Diwu, G. Wu, Z. Chai and S. Wang, *Inorg. Chem.*, 2024, **63**, 12333–12341.
43 J. Yang, W. Liu, M. Xu, X. Liu, H. Qi, L. Zhang, X. Yang, S. Niu, D. Zhou, Y. Liu, Y. Su, J.-F. Li, Z.-Q. Tian, W. Zhou, A. Wang and T. Zhang, *J. Am. Chem. Soc.*, 2021, **143**, 14530–14539.
44 B.-R. Wulan, S.-S. Yi, S.-J. Li, Y.-X. Duan, J.-M. Yan, X.-B. Zhang and Q. Jiang, *Mater. Chem. Front.*, 2018, **2**, 1799–1804.
45 A. Chaturvedi, S. Gaber, S. Kaur, K. C. Ranjeesh, T. C. Nagaiah and D. Shetty, *ACS Energy Lett.*, 2024, **9**, 2484–2491.
46 G. Kresse and J. Furthmüller, *Comput. Mater. Sci.*, 1996, **6**, 15–50.
47 G. Kresse and J. Hafner, *Phys. Rev. B:Condens. Matter Mater. Phys.*, 1994, **49**, 14251–14269.
48 J. P. Perdew, K. Burke and M. Ernzerhof, *Phys. Rev. Lett.*, 1996, **77**, 3865–3868.
49 P. E. Blöchl, O. Jepsen and O. K. Andersen, *Phys. Rev. B:Condens. Matter Mater. Phys.*, 1994, **49**, 16223–16233.
50 G. Kresse and D. Joubert, *Phys. Rev. B:Condens. Matter Mater. Phys.*, 1999, **59**, 1758–1775.
51 Y. Huang, J. Long, Y. Wang, N. Meng, Y. Yu, S. Lu, J. Xiao and B. Zhang, *ACS Appl. Mater. Interfaces*, 2021, **13**, 54967–54973.
52 J.-X. Liu, D. Richards, N. Singh and B. R. Goldsmith, *ACS Catal.*, 2019, **9**, 7052–7064.
53 *CRC Handbook of Chemistry and Physics*, ed. D. R Lide, CRC Press, 90th edn(Taylor and Francis Group), Boca Raton, FL. 2009.
54 H. Hu, R. Miao, F. Yang, F. Duan, H. Zhu, Y. Hu, M. Du and S. Lu, *Adv. Energy Mater.*, 2024, **14**, 2302608.

